Clouds and Water Vapor in the Climate System: Remotely Piloted Aircraft and Satellites

Summary of Research
NASA Langley Agreement NAG-1-1849
July 1, 1996–February 28, 1999

Submitted to
National Aeronautics and Space Administration
from
President and Fellows of Harvard College
c/o Office for Sponsored Research
Holyoke Center, Room 458
1350 Massachusetts Avenue
Cambridge, Massachusetts 02138

James G. Anderson, Principal Investigator
Division of Engineering and Applied Sciences and
Department of Chemistry and Chemical Biology
Harvard University
12 Oxford Street
Cambridge, MA 02138

October 1, 1999

A Final Report: Clouds and Water Vapor in the Climate System: Remotely Piloted Aircraft and Satellites

The objective of this work was to attack unanswered questions that lie at the intersection of radiation, dynamics, chemistry and climate. Considerable emphasis was placed on scientific collaboration and the innovative development of instruments required to address these scientific issues. The specific questions addressed include: *Water vapor distribution in the Tropical Troposphere:* An understanding of the mechanisms that dictate the distribution of water vapor in the middle-upper troposphere; *Atmospheric Radiation:* In the spectral region between 200 and 600 cm^{-1} that encompasses the water vapor rotational and continuum structure, where most of the radiative cooling of the upper troposphere occurs, there is a critical need to test radiative transfer calculations using accurate, spectrally resolved radiance observations of the cold atmosphere obtained simultaneously with *in situ* species concentrations; *Thin Cirrus:* Cirrus clouds play a central role in the energy and water budgets of the tropical tropopause region; *Stratosphere-Troposphere Exchange:* Assessment of our ability to predict the behavior of the atmosphere to changes in the boundary conditions defined by thermal, chemical or biological variables; *Correlative Science with Satellite Observations:* Linking this research to the developing series of EOS observations is critical for scientific progress.

Summary of Progress and Results

The original payload proposed in 1994 and initiated in 1996 underwent a two-stage test phase from NASA Dryden. The first test flights of the radiometer/suntracker occurred on board the NASA ER-2 aircraft in February 1998. In November 1998, the radiometer/suntracker was flown in combination with instruments to measure water vapor, total water, particles and tracers on the ER-2.The Interferometer for Emission and Solar Absorption (INTESA), developed under this research support, is an infrared spectrometer designed to study radiative transfer in the troposphere and lower stratosphere from a NASA ER-2 aircraft. The Fourier transform spectrometer (FTS) operates from 0.7 to 50 μm with a resolution of 0.7 cm^{-1}. The FTS observes atmospheric thermal emission from multiple angles above and below the aircraft. A heliostat permits measurement of solar absorption spectra. The calibration system includes three blackbodies to permit in-flight assessment of radiometric error. In the laboratory, the radiometric accuracy is ~0.1 K in the mid-infrared, an important goal for climate observation from space.

Remote sounding of atmospheric temperature profiles, which is of paramount importance to numerical weather forecasting, has been conducted routinely with the 15 μm CO_2 band using low spectral resolution satellite remote sensors. Next generation atmospheric sounders, such as the Atmospheric Infrared Sounder (AIRS, Aumann and Pagano, 1994), are also designed to use the 15 μm CO_2 band, but in addition will have spectral channels in the 4.3 μm CO_2 R branch. This region is useful because the weighting functions are quite sharp (partially due to the lack of interfering hot bands and isotopes) and because the Planck function is more sensitive to the temperature in the short wave. AIRS has a nominal spectral resolution of 2 cm^{-1} in this region, thus producing a good number of channels with sharp weighting functions.

Like remote sounding using the 15 μm CO_2 band, implementation of the 4.3 μm band sounding requires an accurate forward transmittance model for temperature retrieval. The well-known extreme sub-Lorentz behavior of the CO_2 lineshape in this region is difficult to model, especially inside the bandhead between lines, which is where the best sounding channels are located. Moreover, there are very few studies of the lineshape at low temperatures relevant for atmospheric sounding. Thus, validation of forward model assumptions with in-flight measurements is an important step toward improvements of model and temperature retrieval.

Our approach and preliminary findings from a recent field campaign using a newly developed high-resolution Interferometer for Emission and Solar Absorption (INTESA) flown on the NASA ER-2 were presented at the American Meteorological Society 10th Conference on Atmospheric Radiation, 28 June-2 July 1999, in Madison WI. The observed radiances and transmittances were compared to computed quantities using a new pseudo line-by-line algorithm, kCARTA (Strow *et al.*, 1998). kCARTA uses compressed look-up tables for computation of transmittances and radiances that were derived from the GENLN2 line-by-line code (Edwards, 1992), which uses a parameterization of the 4.3 μm CO_2 lineshape developed by Cousin *et al.* (1985).

The character of the data required to measure decade-to-century scale climatic change is distinctly different from that required for weather prediction or for studies of meteorological processes. The data must possess the accuracy to detect the small secular climate changes of interest. To be useful to future investigators, the data must include convincing proof that a given level of accuracy was in fact attained. An approach founded on the over-determination of instrument calibration, an approach that aims to reveal rather than conceal instrumental error, is shown to be capable of providing convincing accuracy.

Spectrally resolved infrared-radiance is arguably the single most important quantity to measure accurately from space—it contains the fingerprint of both climate response and the forcing that causes it. Kiehl (1983) showed that IR radiance observations could be used directly to detect the climatic response to greenhouse gas forcing. Haskins *et al.* (1999) have demonstrated that IR-radiances can be used to construct powerful tests of the fidelity of climate models. They compare the vertical covariance in temperature and water-vapor predicted by a model with observations of this covariance via a comparison between predicted and observed radiance covariances. By using raw radiance data directly, these methods provide the ability to test models against data that are uncontaminated by a retrieval system.

Enhanced stratospheric ozone depletion in the polar vortices depends on the persistence of temperatures sufficiently low to allow heterogeneous reactions on cold aerosols. Both the temperature of the vortex and the temperature below which these reactions become important depend on the concentration of water vapor, which is determined by the mean mixing ratios of H_2O and CH_4 entering the stratosphere in the tropics ($[H_2O]_e$ and $[CH_4]_e$). Recent work shows that $[H_2O]_e$ is well predicted by the mean saturation mixing ratio of water vapor at the tropical tropopause. While temperatures in most of the stratosphere will cool as greenhouse gas concentrations increase, the tropical tropopause may warm, increasing the saturation mixing ratio and thus $[H_2O]_e$. Several recent studies have predicted substantial increases in arctic ozone

depletion due to the stratospheric cooling induced by increasing CO_2 concentrations. Here we combine GCM predictions of tropical tropopause temperatures with one-dimensional radiative convective model results, recent progress in understanding the stratospheric water vapor budget, modeling of heterogeneous reaction rates and GCM modeling of the radiative impact of increased water vapor to evaluate the effects of greenhouse gas increases on stratospheric water vapor and thus on ozone depletion. Thus, it is shown that ozone loss in the late winter and spring arctic vortex depends critically on water vapor variations forced by sea surface temperature changes in the tropics.

Publications

Hu, H., L. L. Strow, D. W. Keith, and J. G. Anderson, Validation of radiation transfer for atmospheric temperature sensing, *Preprint volume, 10th Conference on Atmospheric Radiation*, 28 June-2 July 1999, Madison WI, American Meteorological Society, June 1999.

Keith, D. W., Climate observation from space: The role of sensor accuracy, *Preprint volume, 10th Conference on Atmospheric Radiation*, 28 June-2 July 1999, Madison WI, American Meteorological Society, June 1999.

Dykema, J. A., D. W. Keith, H. Hu, and L. Lapson, An accurate radiometer for climate observation, *Preprint volume, 10th Conference on Atmospheric Radiation*, 28 June-2 July 1999, Madison WI, American Meteorological Society, June 1999.

Keith, D. W., and J. G. Anderson, Climate observation from space: The role of sensor accuracy, *J. Climate*, submitted March 1999.

Kirk-Davidoff, D., J. G. Anderson, E. J. Hintsa, and D. W. Keith, The impact of climate change on ozone depletion by way of stratospheric water vapor, *Nature*, submitted August 1999.

Keith, D. W., H. Hu,. A. Dykema, L. Lapson, and J. G. Anderson, An airborne interferometer for atmospheric emission and solar absorption, *Applied Optics*, submitted 1999.

An Airborne Interferometer for Atmospheric Emission and Solar Absorption

David W. Keith, Haijun Hu, John A. Dykema, Larry Lapson, James G. Anderson
Harvard University, Department of Earth and Planetary Sciences, Cambridge Massachusetts.

Abstract. The Interferometer for Emission and Solar Absorption (INTESA) is an infrared spectrometer designed to study radiative transfer in the troposphere and lower stratosphere from a NASA ER-2 aircraft. The Fourier transform spectrometer (FTS) operates from 0.7 to 50 μm with a resolution of 0.7 cm^{-1}. The FTS observes atmospheric thermal emission from multiple angles above and below the aircraft. A heliostat permits measurement of solar absorption spectra. The calibration system includes three blackbodies to permit in-flight assessment of radiometric error. In the laboratory, the radiometric accuracy is ~0.1 K in the mid-infrared, an important goal for climate observation from space.

1. Introduction

Analysis of the radiative mechanisms that control the earth's climate, and measurement of long-term secular trends in climate, demand new approaches to the measurement of infrared radiance. With respect to mechanisms, stronger tests of radiative transfer models are needed, both to improve the accuracy of soundings retrieved from the high-resolution radiance spectra to be provided by the next generation of meteorological sounders, and to test the accuracy of radiative cooling rates that are a key driver of tropical meteorology. With respect to climate monitoring from space, sensors are required that have sufficient accuracy to directly determine the small secular trends of interest without relying on the sensor-to-sensor overlap that is necessary with insufficiently accurate instruments. In the mid-infrared this demands a radiometric accuracy of ~0.1 K.

We have designed and tested an Interferometer for Emission and Solar Absorption (INTESA) intended to test models of atmospheric radiative transfer, to detect trace constituents in the troposphere and lower stratosphere, and to serve as a temperature and humidity sounding system. The Fourier transform spectrometer (FTS) covers a spectral range from 0.7 to 50 μm with a resolution of 0.7 cm^{-1}. With overlapping detectors, the instrument has continuous spectral coverage in the 3-50 μm region. It measures atmospheric emission from above and below the aircraft; in addition, it measures the atmospheric absorption in the direct solar beam.

INTESA fills an unusual niche in the evolution of airborne infrared spectrometers. The design of previous airborne infrared spectrometers has focused either on meteorological sounding or on the detection of trace atmospheric constituents. In contrast, INTESA is aimed both at the testing of radiative transfer models and at demonstrating high accuracy radiance measurements that are required for climate observation. Instruments for meteorological sounding typically have a spectral resolution between 0.3 and 3 cm^{-1}, and observe only the most important bands for sounding, from ~4 to 15 μm (e.g., HIS[1], NAST-I[2]). Instruments for detection of trace constituents typically have spectral resolutions at least an order of magnitude higher (e.g., of order 0.01 cm^{-1}) and typically operate either in emission (FIRS[3]) or solar absorption (MarkIV[4]) but not both. INTESA has a resolution comparable to modern sounding instruments (e.g., NAST-I), but has poorer sensitivity and is not designed for cross-track scanning. Unlike a typical sounding instrument INTESA can observe emission at various angles above and below the aircraft, and can also observe the solar beam.

The combination of (1) a spectrometer that can observe radiance above and below the aircraft while also measuring column absorption in the solar beam, with (2) a platform that can operate from the mid-troposphere to the lower-stratosphere, provides a unique and powerful tool to test models of radiative transfer that are the basis of nadir sounding algorithms. The usual

method of testing such systems is to compare nadir radiance measured from an aircraft with that computed based on temperature and humidity profiles measured by a sonde[5]. While this method may be optimal for end-to-end testing of a retrieval system, it is less than optimal for testing the underlying radiative transfer models. INTESA permits an experimental design in which radiance and column absorption are measured on parallel flight tracks at two (or several) altitudes. The resulting data over-constrains the radiation field, allowing analysis to be substantially less sensitive to uncertainties in the atmospheric profile that are often the dominant error in the nadir-only experiment.

The spectral region between 20 and 50 μm has been under-explored by existing air- or space-borne instruments, yet it is the key spectral region for radiative cooling of the upper troposphere. Uncertainty in radiative transfer in this region has significant implications for climate[6]. Experiments with INTESA will examine the spectroscopy of the water-vapor rotation band using the combination of emission and absorption observations described above.

INTESA shares many design features with a spectrometer intended for climate observation from space that was proposed as the centerpiece of the Arrhenius mission[7], which focused on the high-accuracy, spectrally-resolved, measurement of infrared radiation as a method of climate observation[8]. The radiometric calibration system includes three blackbodies, one of which is designed to operate at cryogenic temperatures to provide an accurate zero reference. In the laboratory, INTESA has demonstrated a radiometric accuracy of ~0.1 K in the 300-1500 cm^{-1} spectral range.

Low weight, power consumption, and volume were among the key design goals because INTESA is designed to fly either on a NASA ER-2 high-altitude aircraft or on a remotely piloted aircraft. As flown on the ER-2 in 1998, the total weight of INTESA, including the instrument rack, was 60 kg.

2. Instrument Design

A schematic view of the instrument including optics, detectors, and moving mirrors is shown in Figure 1. Six detectors share the interferometer's two output ports. The spectral range and scientific purpose of each detector is summarized in Table 1. In the following subsections, we first describe the optical design, detectors, and calibration; we then describe the electromechanical systems, first covering the heliostat, then the mechanical design, and finally the electronics and software.

A Optical Design

2.A.1 Fore Optics

The optical system includes a pointing mirror as its first optical element. This mirror allows the spectrometer to view radiation from (1) the atmosphere above or below the aircraft, (2) the blackbodies, or (3) the solar beam reflected by the heliostat.

From scene to detector, ignoring folding mirrors, the optical system is arranged as shown in Figure 2. The fore optics incorporate a three-element image relay. The first mirror forms an image of the scene on the primary field stop. In addition, it images the blackbody aperture onto the second mirror, that acts as a "field lens" and is coincident with the primary aperture stop. The third mirror relays the image of the aperture stop (and the blackbody aperture) through the beam

splitter onto the corner-cube vertex. In relaying the image of the blackbody aperture to the interferometer corner cube vertex, the system has a magnification of 1.2.

The three optic image relay system requires one more optic than the more conventional two-optic telescope. It offers the following advantages: (1) A single aperture stop controls the beam waists at the blackbody aperture and corner cube vertex. (2) The size of the beam waist at the blackbody is as small as is possible, consistent with the etendue of the interferometer and the desired field of view (FOV). Because this system does not place the primary field stop at the detector, it sacrifices some sensitivity but facilitates the achievement of high radiometric accuracy.

All the reflective optics except the heliostat mirrors are diamond machined aluminum with vacuum deposited gold-on-chrome coating (Lumonics Optics, Ottawa Canada). The mirrors are bonded to custom-designed aluminum mirror mounts. Because the heliostat mirrors are exposed to the free air stream and must be handled every flight, they have a more robust coating. It is made by electroplating nickel on the aluminum substrate, diamond machining the surface, and then electroplating ~0.5 μm of gold (Hardric Laboratories, Waltham, MA).

The field stop for the infrared channels is located on a rotating wheel offering six choices of field stop aperture or specialized filter. The FOV may be changed in flight to effect the desired trade-off between SNR and self apodization for a given detector. The filters are required for observation of the solar beam. For the mid-infrared the standard external FOV is 57 mrad full angle—48 mrad FOV at the interferometer after demagnification in the image relay.

2.A.2 Interferometer

The interferometer is a custom Bomem "MB" (Bomem, Quebec, Canada), a permanently aligned right-angle Michelson interferometer. It features corner cubes mounted at right angles to each other on a "wishbone" structure that rotates around the beam splitter so that the cubes move in opposite directions along orthogonal optical axes. Its optical properties are summarized in Table 2. The custom designed beam splitter is CsI with a flatness of $\lambda/5$ at 0.6 μm and a parallelism of ~2 μrad (Spectral Systems, Hopewell Junction, NY). The high index coating material is Si rather than Ge, to allow transmission at 0.75 μm. The coating allows good fringe contrast at 0.75 μm at the expense of diminished performance at longer wavelengths where the reflectivity falls to 10% at 50 μm. The corner cube faces are permanently aligned to an accuracy of 5 μrad and are flat to $\lambda/10$. The only required alignment, the relative position of the two corner cube vertexes, is performed by Bomem at the factory. First-order thermal expansion effects are removed because each arm of the wishbone is of equal length.

The wishbone is an aluminum structure that rotates on a set of steel flexures driven by a solenoidal electromagnet on one of the arms. It has good inherent vibration insensitivity and high mechanical reliability. The system is balanced so that the center of mass is located at the flexure, effectively minimizing the susceptibility to linear vibrations. The interferometer core is mounted kinematically on three titanium bolts that penetrate the optical plate; the core may be easily removed and replaced.

The interferometer is used in the Connes, or four-port, configuration in which the two complementary inputs and outputs are physically separated. One input comes from the pointing mirror via the fore optics. The other input comes from a blackbody source with good short-term stability but no radiometric accuracy. The two outputs feed separate detector systems (Figure 1).

A 0.5 mW linearly polarized HeNe laser in a hermetic vessel provides the optical reference for the interferometer. The HeNe is packaged with its power supply in a cylindrical case, allowing a low weight and low volume pressure vessel.

B Detectors

The spectrometer employs six detectors to cover the spectral range from 0.7 to 50 μm (Table 1). The detectors share the two output ports of the interferometer as shown in Figure 1. The MB- HgCdTe and the InSb share one interferometer output using a dichroic beam splitter. All other detectors share the other port using two moveable mirrors, and a dichroic for the short wavelength Ge and Si detectors. Detector characteristics are summarized in Table 3.

The two HgCdTe detectors and the InSb are mounted in a single Dewar with three optical ports. The liquid nitrogen Dewar offered significant advantages over mechanical cryocoolers including freedom from vibration and electrical pick-up, reliability, and provision of dry nitrogen boil-off.

A pyroelectric detector is used to cover the band from 25 μm, the long-wave cutoff of the HgCdTe detectors, to 50 μm, the long-wave cutoff of CsI. Pyroelectric detectors do not need cooling, are highly reliable, very linear, and offer nearly "black" spectral responsivity. However, they have low detectivity and are sensitive to acoustic noise.

In order to mitigate the influence of aircraft vibrations, the pyroelectric detector is mounted along with its objective mirror on a vibration isolating mount with a resonant frequency of ~35 Hz. Despite the isolator, aircraft vibration significantly degrades the detector performance.

The high linearity of the pyroelectric detector is key to the laboratory demonstration of high radiometric accuracy described in Section 3.A. It serves as a linear standard that allows more robust diagnosis and correction of radiometric error due to non-linearity in the photoconductive HgCdTe detectors.

2.B.1 Detector Optics and Filters

The six detectors employ three different kinds of optical systems. Three cryogenically cooled detectors (two HgCdTe's and an InSb) each use a system like that depicted in Figure 2, in which the final optic is a $f \sim 0.7$ field lens. It is nonimaging to ensure that the sky is not imaged onto the detector. This prevents inhomogeneity in the detector sensitivity from causing inhomogeneity in the system responsivity across the FOV. This is important for achieving a symmetric instrument line shape function. The shape and placement of the field lens is optimized using three-dimensional ray tracing to meet the twin constraints of minimizing the beam spot on the detector while ensuring that rays from each point in the sky are distributed evenly across the detector surface.

Two solar band detectors, the Si and Ge photodiodes, share a 100 mm focal-length glass lens. A dichroic beam splitter located upstream from the lens' focus divides light between the two detectors. Unlike the other detectors in the system, the field stop for both Si and Ge detectors is the 1 mm diameter active area of each detector. The detectors are co-aligned on an optical bench, and have measured FOVs of 12 and 9.3 mrad respectively.

The DTGS detector is located at the focus of a 44 mm diameter parabolic mirror with a 38 mm focal length. The FOV of the detector/mirror system is large enough that light reaching the detector from the scene is controlled by the primary field stop in the fore optics.

C Radiometric Calibration System

The radiometric design is constrained by the twin goals of (1) high radiometric accuracy on bright sources, primarily nadir views, and (2) low zero offset needed for looking at thin clouds above the aircraft. To realize these goals the instrument carries three blackbodies. Two "warm" blackbodies, maintained at ~240 and ~310 K, bracket the range of observed nadir brightness temperature allowing optimal calibration for the non-linear photoconductive detectors. Accurate determination of radiometric zero demands a cryogenic blackbody, because the equivalent temperature of a typical thin cirrus cloud at 900 cm^{-1} is ~120 K. Most importantly, use of three blackbodies allows in-flight estimation of end-to-end radiometric error.

The warm blackbodies are each built around an aluminum tube with a 120° opening-angle concave cone at its end. The blackbodies have an entrance aperture of 2.5 cm, an interior diameter of 3.5 cm and a length of 7.5 cm giving an aperture to length aspect ratio of ~3. The interior surfaces are treated by Enhanced Martin Black (Lockheed-Martin, Denver, CO) which has a total reflectance of less than 3% between 3 and 50 μm. The estimated on-axis emissivity is >0.998. To achieve temperature uniformity, the blackbody is suspended only by its entrance end using a low conductivity mount. The blackbodies are heated using thermofoil heaters, and are insulated with ~1.5 cm of Nomex and polyimide foam. Thermostatic control is accomplished in software. Temperatures are measured at four points along the blackbody. Temperature uniformity in flight is ~0.5 K between the midpoint of the blackbody cylinder and the endcap when the blackbody is ~100 K warmer than ambient.

The cryogenic blackbody core is 10 cm long, but is otherwise similar to the blackbody cores described above. Its estimated[9] on-axis emissivity is >0.999. The blackbody Dewar permits direct access to the blackbody core which is mounted in a toroidal liquid nitrogen vessel. The Dewar is 15 cm diameter by 15 cm long with a dry mass of 2.7 kg, and a hold time of ~30 hr. Both blackbody and detector Dewars were supplied by Kadel Engineering, Danville, IN. Ice build up, and the creation of ice or liquid fog, are prevented by a shutter mounted on the face of the Dewar in combination with a continuous purge of dry nitrogen provided by boil-off from the Dewar. In operation, a dry nitrogen purge is established prior to Dewar filling, and the shutter is opened only when required for calibration.

Blackbody temperatures are measured using high-stability thermistors ("super-stable, 4600 series", YSI, Yellow Springs, OH). When operated at <70 °C these thermistors have a temperature drift of <0.01 °C in 8 years. Primary temperature calibration to NIST traceable standards was performed by YSI. Accuracy was checked by comparing YSI thermistors with different resistances, β-coefficients, and encapsulation technologies, and by comparison with thermistors supplied by other vendors. Comparisons with several thermistors on an isothermal mount demonstrated that the end-to-end system accuracy—including readout electronics—was better than 0.05K. The readout electronics compare the thermistors with reference resistors that have an accuracy of 250 ppm and a temperature coefficient of 10 ppm K^{-1}. The effects of reference voltage drift, or drift in ADC gain are thus eliminated to first order.

D Heliostat

The heliostat directs the solar beam into the instrument via the pointing mirror. The optical design allows the tracking of the overhead solar beam to solar zenith angles of 50° to 70°, depending on aircraft heading. The design differs from that of heliostats for balloon borne instruments that are typically designed to look near the horizon[10]. The tracking is achieved by

two independent mirrors, a design which affords overall compactness and is also lightweight. Each mirror is driven by a stepper motor with a micro-stepper drive that has a resolution of 0.1 mrad. The heliostat optomechanical assembly weighs a total of 1.7 kg, with an additional 1.1 kg for the associated electronics.

The heliostat is positioned in an opening in the skin of the ER-2 superpod which necessitates its removal when loading or unloading the instrument. A kinematic mounting system assures angular repeatability of <1 mrad for each installation of the heliostat assembly. The opening in the superpod skin exposes the heliostat to the airstream during flight, requiring thermal control for the motor and bearing assemblies. This is achieved with thermofoil heaters.

A pickoff mirror directs a small portion of the solar beam through a lens that images it onto the face of a position sensitive detector (PSD) from Hamamatsu Photonics of Bridgewater, NJ. This sensor allows a servo loop to keep the solar beam aligned along the optical axis.

Servo control is achieved by a digital control loop implemented at 10 Hz. The control loops for the two axes operate independently. The control algorithm includes procedures to locate the solar beam by a raster scan over the entire solid angle visible to the heliostat, and to actively servo the mirrors to lock the solar beam parallel to the optical axis. The PSD detects the solar beam when it is within 100 mrad of the optical axis, allowing the heliostat to typically locate and lock on to the sun in < 1 min.

During typical flights, the heliostat locked on the solar beam for 50-90% of the flight time, depending on the details of the flight path. The typical RMS pointing noise of 4 mrad compared to solar image size of 9 mrad and instrument FOV of ~50 mrad.

E Environmental Control and Gas Handling

The use of hygroscopic optics (CsI), needed to extend the spectral range to 50 μm, requires that the interior of the instrument maintain good thermal stability and low relative humidity. Thermal control is effected using multiple thermofoil heaters (Minco Products, Inc, Minneapolis, MN), arrayed in three zones surrounding the warm instrument enclosure. Each zone has a maximum power of ~100 W. Temperatures in the warm enclosure are monitored with 15 thermistors. The thermostatic control is in software (with a hardware backup) to allow simple adjustment of the zones to achieve maximum thermal uniformity.

Boil-off of nitrogen from the Dewars provides ~1 STP L/min of dry gas to purge the optics. A single regulator maintains the Dewars at 1 bar pressure. The regulator is an active system comprising an absolute pressure transducer, control electronics, and a solenoid valve packaged with redundant "burst-disks" to protect against over-pressure. Flow from the regulator is split between the warm enclosure (where it is directed onto the interferometer beam splitter), the cold side of the bulkhead window, and the cryogenic blackbody.

In an unpressurized system, substantial purge flow is required to keep the optics dry during rapid descent from the cold upper troposphere. Use of Dewar boil-off for purging was a key design decision. Dewars hold much more gas per unit flown weight than do high pressure bottles. An alternative design would have used mechanical cryocoolers for the detectors and a hermetically sealed instrument enclosure that required no purge gas (e.g., NAST-I [2]). For INTESA, the combination of Dewars and an unpressurized instrument housing saved substantial weight.

F Mechanical design

INTESA is designed to fly in the rear of an NASA ER-2 "super-pod" or in the nose payload bay of an Aurora Perseus remotely piloted aircraft (Aurora Flight Sciences Corp., Manassas, VA). The INTESA system comprises four units, the instrument (36 kg), heliostat (3 kg), flight computer (7 kg), and the aircraft interface box (3 kg). The computer and aircraft interface are described in the following subsection. As flown on the ER-2 in 1998, the total instrument weight including the instrument rack and all electrical cabling was 60 kg.

All components of the instrument are mounted on a single structural plate oriented normal to the direction of flight (Figure 3). The 71 by 58 cm plate is fabricated with graphite-reinforced epoxy face sheets on a 2.5 cm thick aluminum honeycomb core (Zivko Aeronautics, Guthrie, OK). The forward facing side of the plate contains the fore-optics, interferometer, all detectors, and various interface electronics all contained in an environmentally controlled enclosure. The enclosure is 1.2 cm thick, fabricated with graphite face sheets on a foam core. The aft side of the plate holds the pointing mirror, blackbodies, and heliostat.

Stepper motors are used for the pointing mirror, heliostat mirrors, and FOV wheel. The motors are operated with micro-stepping drivers (Intelligent Motion Systems, Inc, Marlborough, CT). Position reference is provided by optical switches in each assembly. At instrument start, and periodically thereafter, the motors are driven until a switch transition is detected to provide a position reference. Typical angular accuracy is ±2 mrad. The shutter on the cryogenic blackbody and the two switch mirrors in the optical system use brushless DC motors with an integrated gearbox and controller (API Portescap, Switzerland).

The instrument is mounted to the ER-2 instrument rack using shock damping mounts with a resonant frequency of ~50 Hz. Two retractable doors are mounted on the ER-2 fairing to protect the heliostat and zenith view ports from the elements during ground operations and low altitude flight.

G Electronics

The flight computer is a 100 MHz i486 single board computer that supports a stack of five custom PC-104 format interface cards. The computer uses a 1.2 GByte 2½ inch-format hard drive in a pressure vessel. Together the interface cards provide 80 analog inputs (12-bit resolution), 20 analog outputs, 100 digital input/outputs, and interface electronics for 12 stepper motors. The high rate interferogram data are delivered from the Bomem sampling electronics over a RS422 link to a Bomem supplied IAS-bus card in the flight computer.

The flight computer, a main signal distribution panel, and DC-to-DC power supplies are contained in a single enclosure with volume of ~30 L and a mass of 6.5 kg. Control of aircraft power and the cockpit interface are handled in a separate smaller box. All other instrument interface electronics, including the Bomem supplied boards, are located in warm enclosures on the instrument structural plate.

Closed loop control of the interferometer scan arm is accomplished by a Bomem supplied board that also includes the 16-bit ADC for sampling interferograms. The pre-amplifiers are a modified Bomem design with digital gain control. A custom multiplexer board after the pre-amplifiers permits two detector channels to be sampled at once, each at one sample every two laser fringes (normally 40 kHz). This board permits selection of any two of the six detector channels under software control.

The instrument operates on 28 V aircraft power. In the ER-2 configuration a cockpit switch operates a relay in the INTESA aircraft interface box that supplies switch power to the instrument. Independent of the state of the relay, the instrument draws "keep alive" power for thermostatic heaters as long as aircraft wing power is present. The mean power requirement is 600 W.

H Flight Software

The flight software runs under the QNX real-time, multitasking operating system. Custom compilers and support software built around a data-flow architecture allow high level instrument control algorithms to be modular and to execute closed-loop control of many separate subsystems running at different rates. For example, the flight algorithm sequences observations of various detectors and pointing mirror targets (blackbodies, sky, heliostat) while simultaneously maintaining closed-loop thermal control of five subsystems at ¼ Hz and closed-loop control of the heliostat at 10 Hz.

On the ER-2, the instrument operates completely autonomously with no telemetry. The only communication is with the pilot via a single "fail light". The software supports telemetry and remote command capability, a facility we expect to use future missions.

The software schedules observation sequences based on flight data, primarily aircraft altitude, as determined by an onboard pressure transducer. For example, less observing time is devoted to zenith observations when the aircraft is at high altitude, and observations are focused on the column absorption measurements using the heliostat when the aircraft is climbing or descending. Control of observation sequencing is readily changed according to the science objectives of a given flight.

3. Performance

To date INTESA has made 9 flights on two ER-2 deployments. Electrical, environmental, and computer systems have all performed well. The most serious problem has been the performance of the DTGS pyroelectric detector. Despite the vibration isolation system, the SNR has not been satisfactory to accomplish the science goals. At present we are considering retrofit of a liquid He cooled Dewar to permit use of solid-state photoelectric detectors. In the remainder of this section we present some representative data and discuss the radiometric calibration.

A Radiometric Calibration

Systematic errors in the radiometric calibration of INTESA were investigated using the instrument's three-blackbody calibration system supplemented with an external laboratory blackbody designed to exceed the performance of the internal blackbodies. The estimated [9] emissivity of the laboratory blackbody is >0.9995. Temperature homogeneity within the core is better than 0.05 K, and thermometric error was <0.03 K. To avoid atmospheric absorption, experiments were performed in a dry nitrogen atmosphere.

End-to-end instrumental errors are assessed by comparing the measured temperature of a blackbody with its radiance—expressed as brightness temperature—as measured by the calibrated instrument. The instrument's calibration is in turn derived from the observation of at least two other blackbodies using blackbody phase correction[11]. An overall radiometric error of

better than 0.15 K was achieved across the spectral region from 300 to 1500 cm^{-1} (Figure 4), equivalent to a relative error in radiance of ~10^{-3} in the mid-infrared.

The laboratory accuracy achieved here is comparable to that achieved by the University of Wisconsin AERI instrument[12] in calibration tests against a NIST blackbody. The AERI-NIST test[13] demonstrated radiometric consistency of 0.03 K, with the NIST blackbody at 303 K. In comparison, the INTESA calibration spans a ~10 times larger temperature range and has errors about 3 times larger.

Laboratory test relying on the linearity of the DTGS detector demonstrate the instruments intrinsic radiometric accuracy, thus allowing accurate characterization and correction of the non-linearity in the MB-HgCdTe detector. After applying non-linearity corrections to the flight data, the instrument achieved its design goal of 0.5 % radiometric accuracy in the 425 to 3000 cm^{-1} spectral range using the LW and MB HgCdTe and the InSb detectors. Poor performance of the DTGS detector prevented in-flight validation in the 200-425 cm^{-1} region.

B Representative Data

Figure 5 shows calibrated nadir emission spectra. The broad, 4 to 50 μm spectral range of these emission spectra allows direct comparison of nadir sounding between the 4 and 15 μm bands of CO_2 and between the rotational and the 6.7 μm bands of H_2O. Figure 6 shows the sensitivity of the instrument in emission mode. Figure 7 shows absorption spectra recorded with the heliostat. In the top panel the data is on a log scale to demonstrate the SNR of ~500:1 in 1 second at 1 cm^{-1} resolution. The absorption data has been used to detect trace constituents, such as HDO and CO in the upper troposphere, and to test the temperature dependence of absorption in the 4.3 μm CO_2 band-edge that is of critical importance for atmospheric sounding[14]. The ability to take the ratio of absorption spectra measured at different altitudes in order to measure absorption in an atmospheric layer bracketed by two aircraft flight tracks is key to these analyses.

4. Summary

We have demonstrated an airborne interferometric spectrometer with a novel combination of features. The instrument can provide new data on the radiative properties of thin cirrus clouds, and new tests of radiative transfer in the water-vapor rotation band. Analysis of solar absorption spectra provide a new measurement of overhead O_3 from the ER-2 that is of key importance to observing missions aimed at stratospheric chemistry, and will provide unique measurements of HDO in the tropical troposphere, where HDO to H_2O ratios can provide new insight into the processes that control the distribution of upper tropospheric humidity.

Robust measurement of secular trends in climate demands space-based sensors with high radiometric accuracy[8]. Radiometric accuracy was a key design goal of INTESA. In the laboratory, the instrument has demonstrated a radiometric accuracy of ~0.1 K over the 300-1500 cm^{-1} spectral region using DTGS pyroelectric detectors with high intrinsic linearity. The results suggest that an FTS using pyroelectric detectors and a similar optical system to that demonstrated on INTESA, could provide high-accuracy climate observations from space[7].

Acknowledgments. We depended on the strengths of the Harvard engineering team; we thank Norton Allen, Joe Demusz, Mike Greenberg, Jim Oliver, Marco Rivero, and Eileen Schomp. We thank Henry Buijs and Andre Villemaire at Bomem for their expert guidance. We thank the ER-2 pilots, Jim Barrilleaux, Ken Broda, Bill Collette, Jan Nystrom, and Dee Porter, as

well as the crew for their unequaled professionalism. Finally we thank our scientific collaborators, Danny Kirk-Davidoff and Ryan Spackman, and one anonymous reviewer. This work was supported under NASA grant NAG-1-1849.

Figure Captions

Figure 1. Schematic of the full optical system. All transmissive optics and moving mirrors are indicated. Numerous flat folding mirrors are omitted, as are the focusing mirrors for the infrared detectors (shown as "Optic 4" on Figure 2). A more detailed layout of the fore optics and interferometer is found in Figure 2. The schematic substantially distorts the system geometry, for example, the three cryogenically cooled detectors, the "InSb", "15 micron HgCdTe", and "25 micron HgCdTe" are located in the same detector Dewar.

Figure 2. Schematic of the optical system for a single cryogenic detector. All folding mirrors, except those in the interferometer core are omitted. Optics 1-4 are illustrated as thin lenses but all are, in fact, mirrors with spherical or parabolic surfaces. The schematic shows the layout of the Bomem MB interferometer projected onto a single plane. In fact the beam exiting the interferometer is translated into the page one beam diameter so that Optic 4 and the detector are on a different plane from Optics 1-3.

Figure 3. Mechanical layout of INTESA showing components on both sides of the optical plate. The illustration is derived from CAD drawings, so the geometry is exact—note the 10 cm scale key.

Figure 4. Laboratory data showing radiometric error as a function of wave number. The instrument was calibrated using blackbodies at 316 and 77 K. Data shows the error when viewing a third blackbody at 287 K, obtained by subtracting the measured blackbody temperature from the equivalent temperature of the measured radiance. The jagged line shows the data at the raw resolution of ~2 cm^{-1}, the smooth line show data at a resolution of ~25 cm^{-1}. The mean equivalent temperature offset across the 300-1500 cm^{-1} band is 0.12 K. The fact that the error is roughly constant across the band suggests that the leading residual error is due to thermometry rather than to a radiance offset or a non-linearity.

Figure 5. Cloud free nadir spectra from cruise altitude over the Pacific. The data are from 17°N 121°W at 21 km altitude, except the DTGS data that is an average for the entire flight. The key at the bottom indicates which of four detectors is plotted, where "LW" and "MB" are the 25 and 15 μm cut-off HgCdTe detectors.

Figure 6. Measured noise equivalent spectral radiance (NESR) the infrared detectors. NESR is in units W cm^{-2} sr^{-1} $(cm^{-1})^{-1}$ at a spectral point spacing of 0.5 cm^{-1} (un-apodized resolution of ~0.7 cm^{-1}) with 1 sec total interferogam acquisition time. Data is from the laboratory, flight results differ by no more than 30%, except for the DTGS. Typical flight spectra are recorded with 8 sec integration giving 2.8 times lower NESR.

Figure 7. Solar absorption spectra. The upper panel shows raw signal in arbitrary units on a log scale *vs* wave number measured using the InSb detector from altitude of 9.9 km with a solar zenith angle of 56°. The absorption minima at 2300 cm^{-1} is bounded by N_2O absorption to the red and the "4.3" μm CO_2 edge to the blue. The CH_4 is visible between 2900 and 3100 cm^{-1}. The lower panel shows the *A*-band of atmospheric O_2 at 0.76 μm observed from the surface.

References

[1] H. E. Revercomb, D. D. LaPorte, W. L. Smith, H. Buijs, D. G. Murcray, F.J. Murcray, and L. A. Sromovsky, "High-altitude aircraft measurements of upwelling IR radiance: prelude to FTIR from geosynchronous satellite," *Mikrochim. Acta*, 2, p.439-444 (1988).

[2] D. Cousins and W. L. Smith, "National Polar-Orbiting Operational Environmental Satellite System (NPOESS) Airborne Sounder Testbed-Interferometer (NAST-I)," *SPIE*, 3127, 323-331 (1997).

[3] D. G. Johnson, K. W. Jucks, W. A. Traub, and K. V. Chance, "Smithsonian stratospheric far-infrared spectrometer and data reduction system," *J. Geophys. Res.*, 100, 3091-3106 (1995).

[4] G. C. Toon, "The JPL MkIV Interferometer," *Opt. and Phot. News*, 2, 19-21 (1991).

[5] L. L. Strow, D.C. Tobin, W. W. McMillan, S. E. Hannon, W. L. Smith, H. E. Revercomb, and R. O. Knuteson, "Impact of a new water vapor continuum and line shape model on observed high resolution infrared radiances," *J. Quant. Spectro. Rad. Trans.*, 59, 303-317 (1998)

[6] A. Sinha and J. E. Harries, "The Earth's clear-sky radiation budget and water vapor absorption in the far infrared," *J. Clim.* 10, 1601-1614 (1997).

[7] J.G. Anderson, et al., "Arrhenius: A small satellite for climate research," NASA proposal ESSP-II-0030. Available from the authors or at "http://www.arp.harvard.edu/sci/rad/arrhenius" (1996).

[8] D. W. Keith "Climate Observation from Space: The Role of Sensor Accuracy", *10th Conference on Atmospheric Radiation*, June 1999, Madison WI, American Meteorological Society, Boston, MA.

[9] R. J. Chandos and R. E. Chandos, "Radiometric properties of isothermal diffuse wall cavity sources," *Appl. Opt.*,13, 2142-2151 (1974).

[10] T. Hawat, C. Camry-Peyret and R. Torguet, "Suntracker for atmospheric remote sensing," *Opt. Eng.* 37, 1633-1642 (1998).

[11] H. E. Revercomb, H. Buijs, H. B. Howell, D. D. Laporte, W. L. Smith, and L. A. Sromovsky, "Radiometric Calibration of IR Fourier-Transform Spectrometers - Solution to a Problem With the High-Resolution Interferometer Sounder," *Appl. Opt.*, 27, 3210-3218 (1988).

[12] H. E. Revercomb, F. A. Best, R. G. Dedecker, T. P. Dirkx, R. A. Herbsleb, R. O. Knuteson, J. F. Short, and W. L. Smith, "Atmospheric Emitted Radiance Interferometer (AERI) for ARM," *Fourth Symposium on Global Change Studies*, January 1993, Anaheim, California, American Meteorological Society, Boston, Mass.

[13] Hank Revercomb, personal communication, 1999. The results are reported in R. Kannenberg, "IR Instrument Comparison Workshop at the Rosenstiel School of Marine and Atmospheric

Science (RSMAS)," *The Earth Observer*, EOS Project Science Office, May/June 1998, Vol. 10 No. 3.

[14] H. Hu, L. L. Strow, D. W. Keith, and J. G. Anderson, "Validation of Radiative Transfer for Atmospheric Temperature Sensing," *10th Conference on Atmospheric Radiation*, June 1999, Madison WI, American Meteorological Society, Boston, MA. Other representative data and analysis may be found at "http://www.arp.harvard.edu/sci/rad/INTESA"

Table 1. Summary of detectors

Detector Name	Spectral window (cm^{-1})	Spectroscopic interest
Silicon	13120±500	Oxygen A-band for sounding cloud properties in reflected solar light.
Germanium	6500-7600	Water band at 1.38 μm for sounding cloud properties in reflected solar light.
InSb	1800-3500	Detection of HDO and other trace constituents in absorption. Emission and absorption from 4.3 μm CO_2 band.
MB-HgCdTe 15 μm cut-off	700-1800	Window, 6.7 μm H_2O, O_3, and blue edge of 15 μm CO_2. Primarily in emission mode.
LW-HgCdTe 25 μm cut-off	400-700	15 μm CO_2 and blue edge of H_2O rotation band. Emission only.
DTGS	200-400	H_2O rotation band.

MB- and LW-HgCdTe denote "mid-band" and "long-wave" HgCdTe detectors.

Table 2. Summary of FTS optical properties

Beam diameter at corner cube vertex (cm)	2.5
Max half angle at corner cube vertex (m rad)	25
Etendue (cm^2 sr)	0.04
Beam splitter material	CsI
Rate of change of OPD ($cm\ sec^{-1}$)	1 or 5
Fringe rate for 632 nm laser (kHz)	16 or 80
Maximum OPD (cm)	±1.0
Unapodized resolution (cm^{-1})	0.60

Table 3. Detector Specifications

Detector	D^* or NEP (1)	Cutoff	Dimensions	Type	Vendor
Si	7×10^{-16} NEP	1.0 μm	1 mm dia	PV	Hamamatsu, Bridgewater N. J.
Ge	3×10^{-13} NEP	1.8 μm	1 mm dia	PV	EG&G Judson, Montgomeryville, PA
InSb	1.4×10^{11} D*	5.5 μm	1.5 mm dia	PV	EG&G Judson,
MB-HgCdTe	4.4×10^{10} D*	15 μm	.1 mm sq	PC	Belov Technology, New Brunswick, NJ
LW-HgCdTe	4.7×10^{9} D*	26.5 μm	2 mm sq	PC	EG&G Judson
DTGS	3.0×10^{8} D*	NA	2 mm dia	Pyro	GEC-Marconi Southampton, UK

(1) D^* has units of cm $Hz^{1/2}$ W^{-1}, and NEP has units of W $Hz^{-1/2}$. All values are at a frequency of 1 kHz.

F 1

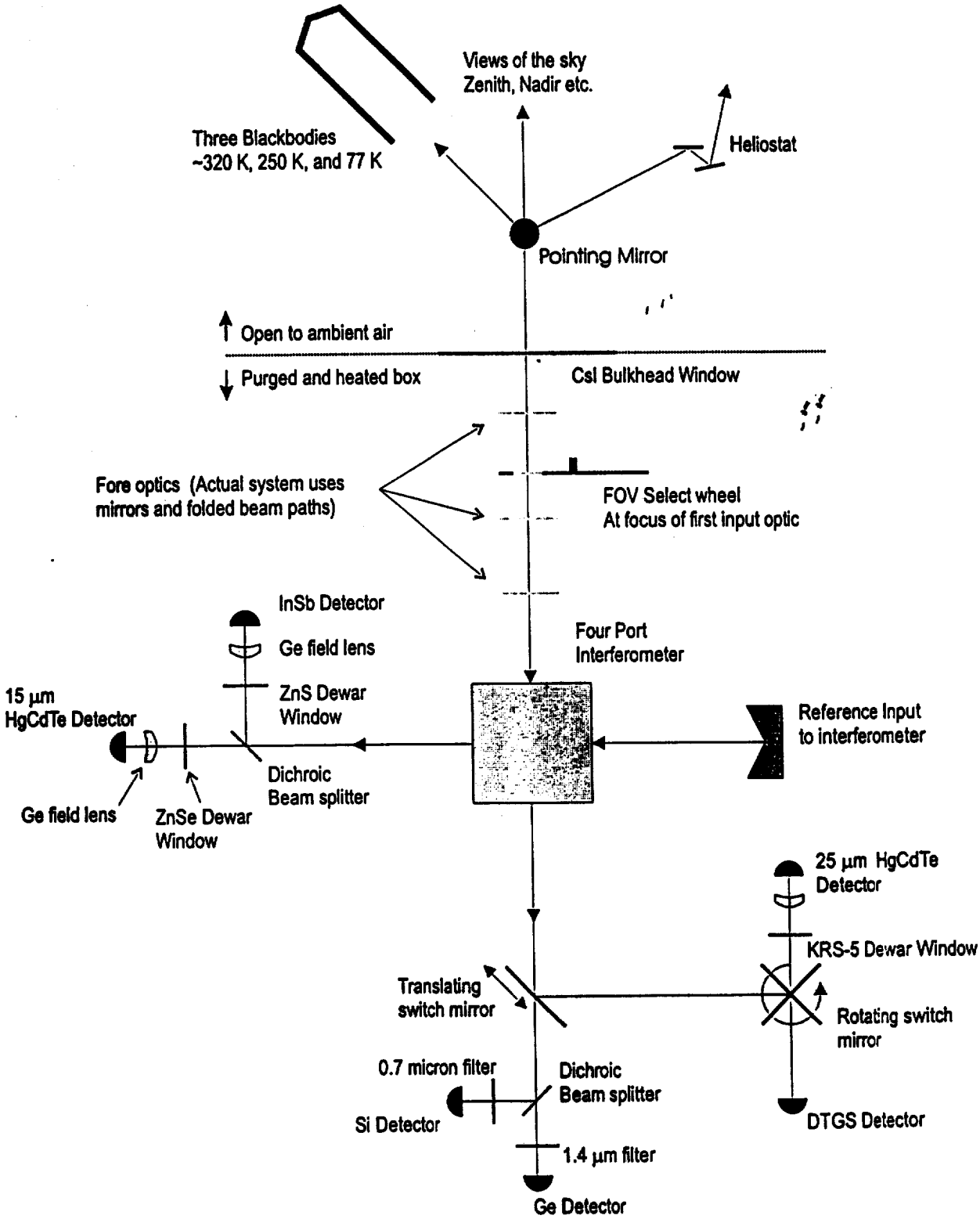
Views of the sky
Zenith, Nadir etc.
Three Blackbodies
~320 K, 250 K, and 77 K
Heliostat
Pointing Mirror
Open to ambient air
Purged and heated box
CsI Bulkhead Window
Fore optics (Actual system uses mirrors and folded beam paths)
FOV Select wheel
At focus of first input optic
InSb Detector
Ge field lens
ZnS Dewar Window
Four Port Interferometer
15 µm HgCdTe Detector
Reference Input to interferometer
Dichroic Beam splitter
Ge field lens
ZnSe Dewar Window
25 µm HgCdTe Detector
KRS-5 Dewar Window
Translating switch mirror
Rotating switch mirror
0.7 micron filter
Dichroic Beam splitter
Si Detector
DTGS Detector
1.4 µm filter
Ge Detector

F 2

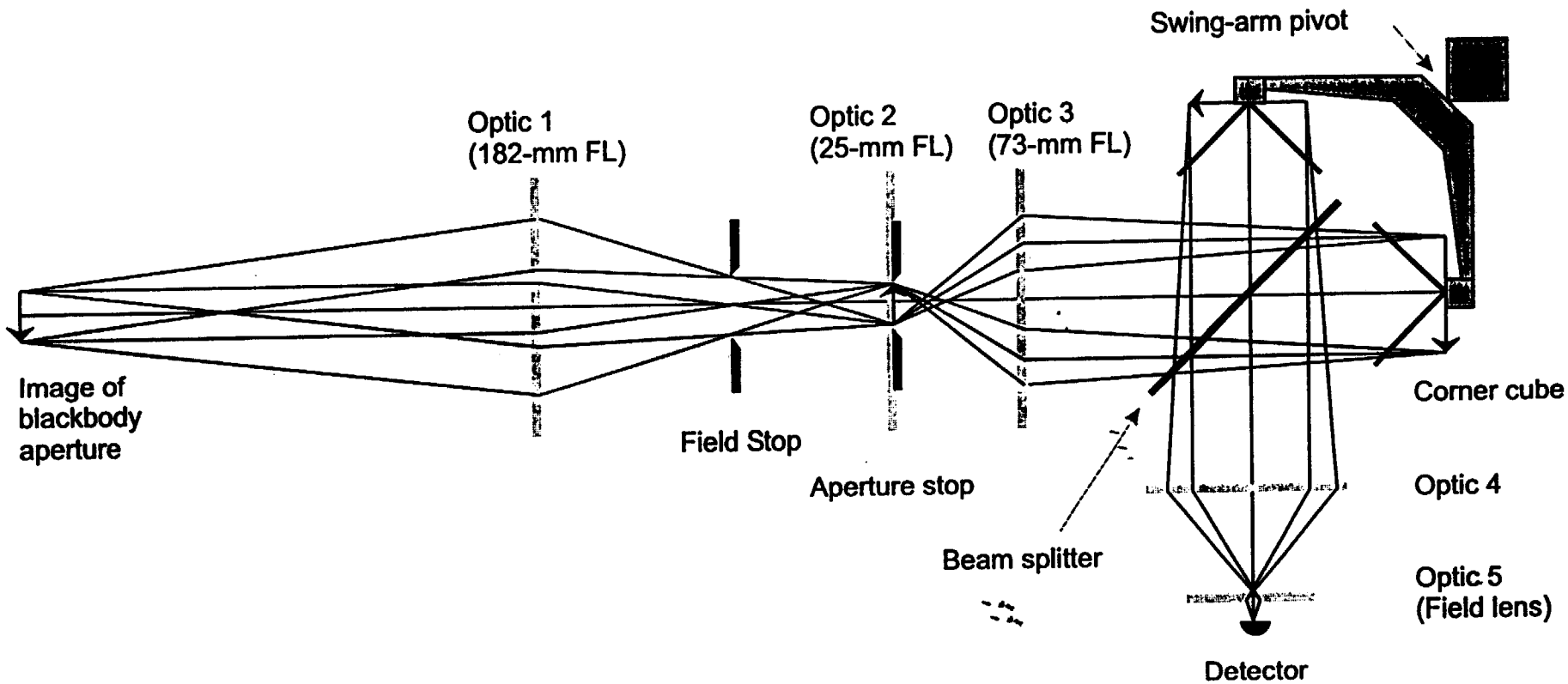
Swing-arm pivot
Optic 1
(182-mm FL)
Optic 2
(25-mm FL)
Optic 3
(73-mm FL)
Image of
blackbody
aperture
Field Stop
Aperture stop
Beam splitter
Corner cube
Optic 4
Optic 5
(Field lens)
Detector

F3

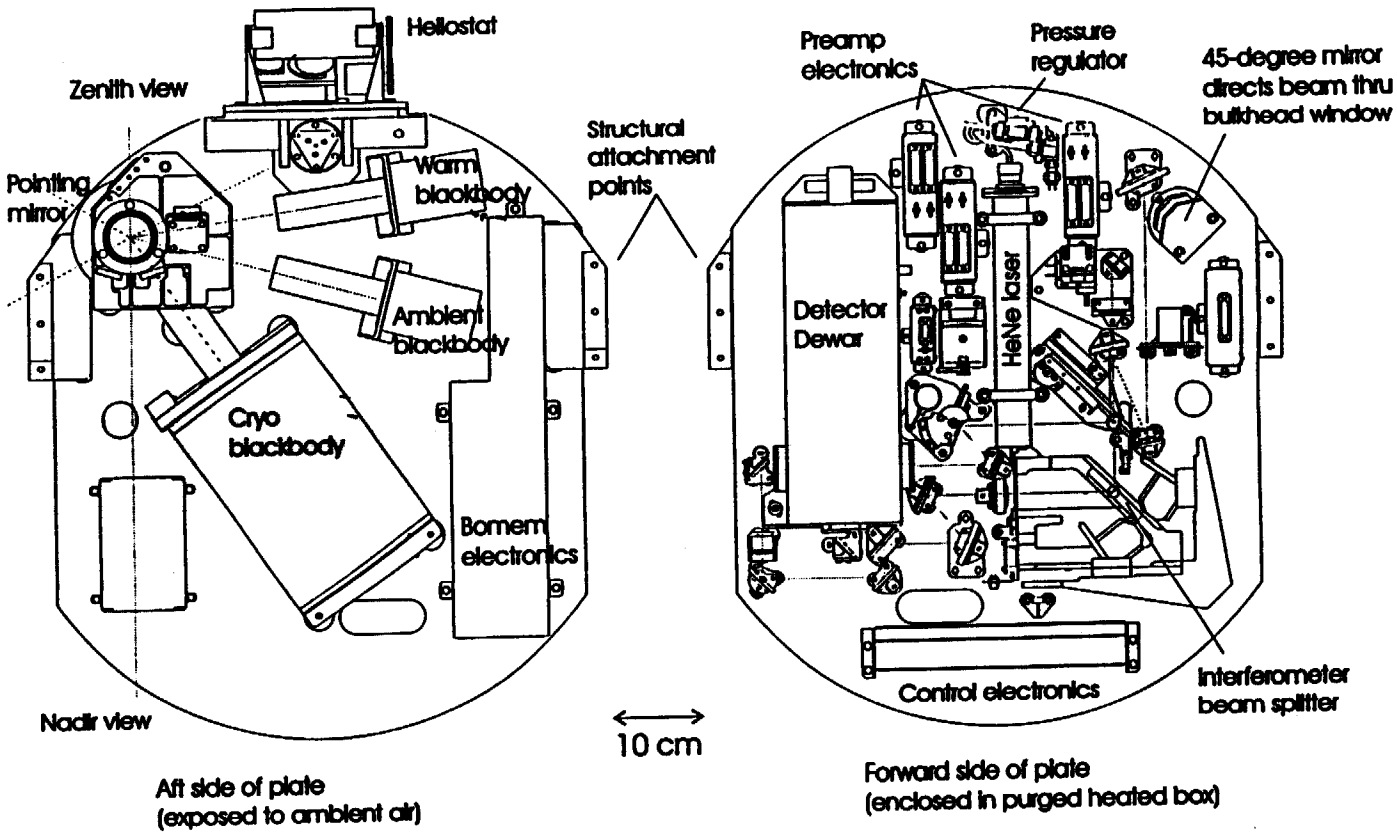
Hellostat
Zenith view
Pointing mirror
Warm blackbody
Ambient blackbody
Cryo blackbody
Bomem electronics
Nadir view
Structural attachment points
10 cm
Preamp electronics
Pressure regulator
45-degree mirror directs beam thru bulkhead window
Detector Dewar
HeNe laser
Control electronics
Interferometer beam splitter
Aft side of plate
(exposed to ambient air)
Forward side of plate
(enclosed in purged heated box)

F4

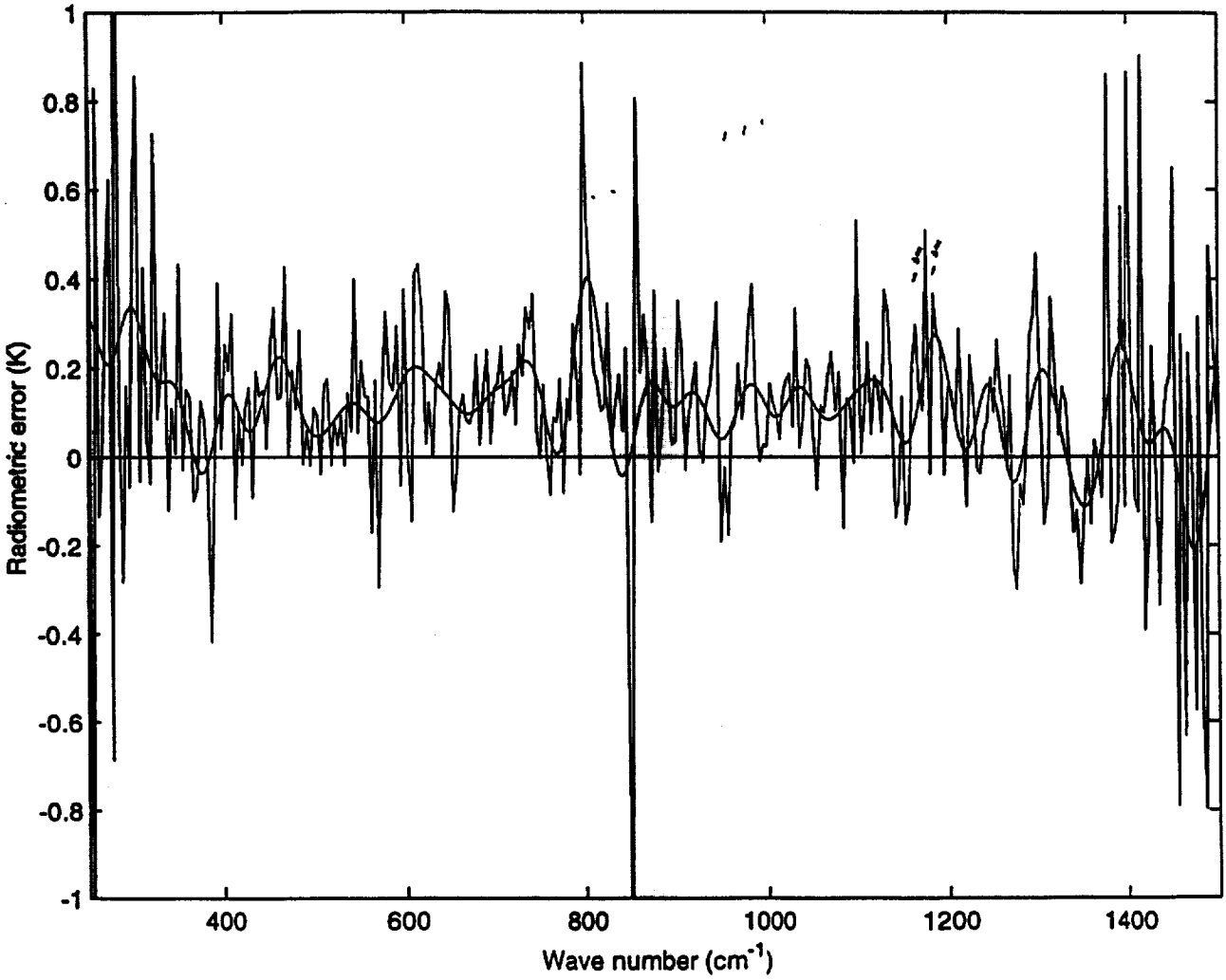
Radiometric error (K)
1
0.8
0.6
0.4
0.2
0
-0.2
-0.4
-0.6
-0.8
-1
400
600
800
1000
1200
1400
Wave number (cm-1)

F5

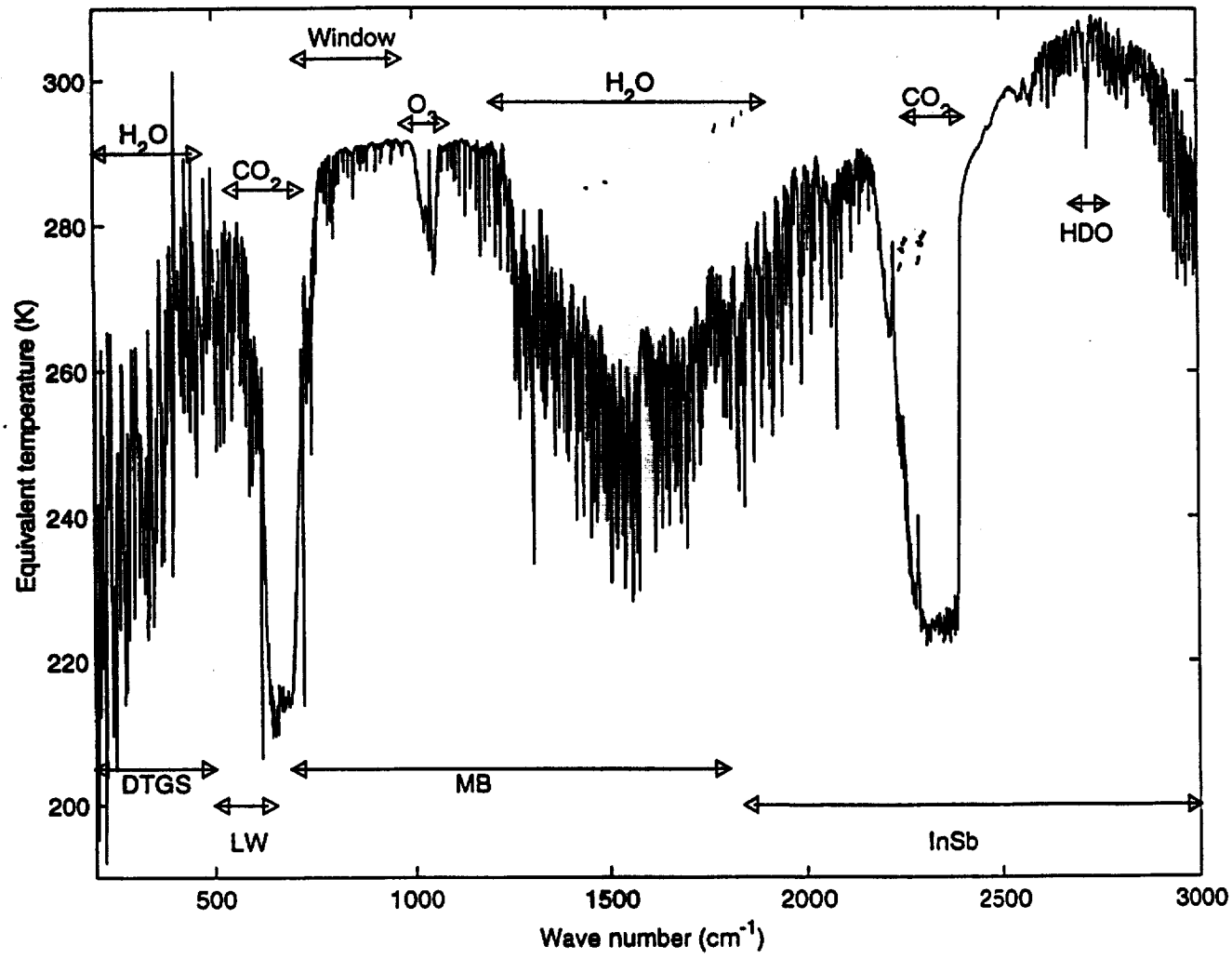
Window
H_2O
O_3
H_2O
CO_2
CO_2
H_2O
HDO
DTGS
LW
MB
InSb
Equivalent temperature (K)
300
280
260
240
220
200
500
1000
1500
2000
2500
3000
Wave number (cm^{-1})

F6

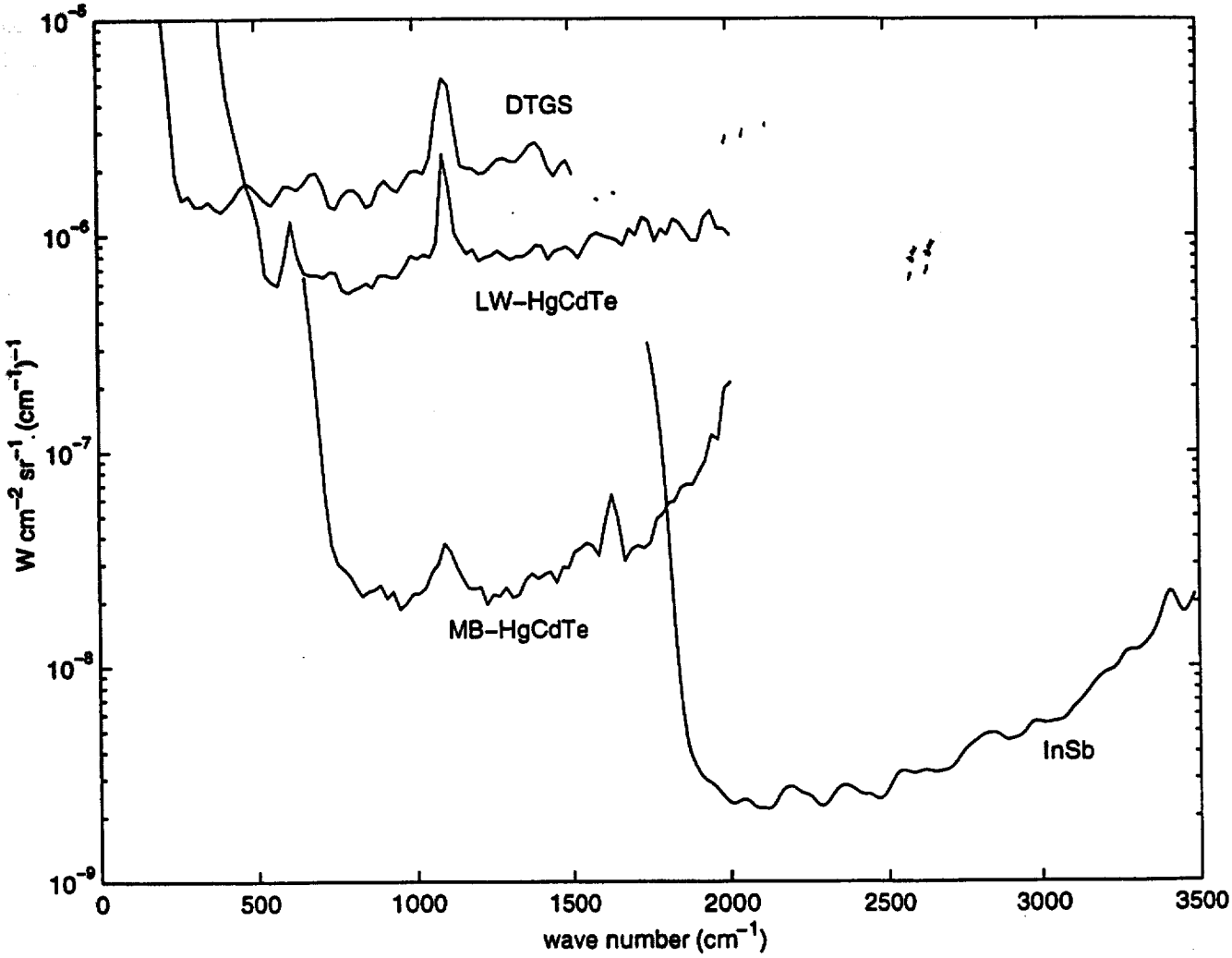
DTGS
LW-HgCdTe
MB-HgCdTe
InSb
W cm^{-2} sr^{-1}.(cm^{-1})$^{-1}$
wave number (cm^{-1})
10^{-5}
10^{-6}
10^{-7}
10^{-8}
10^{-9}
0
500
1000
1500
2000
2500
3000
3500

F7

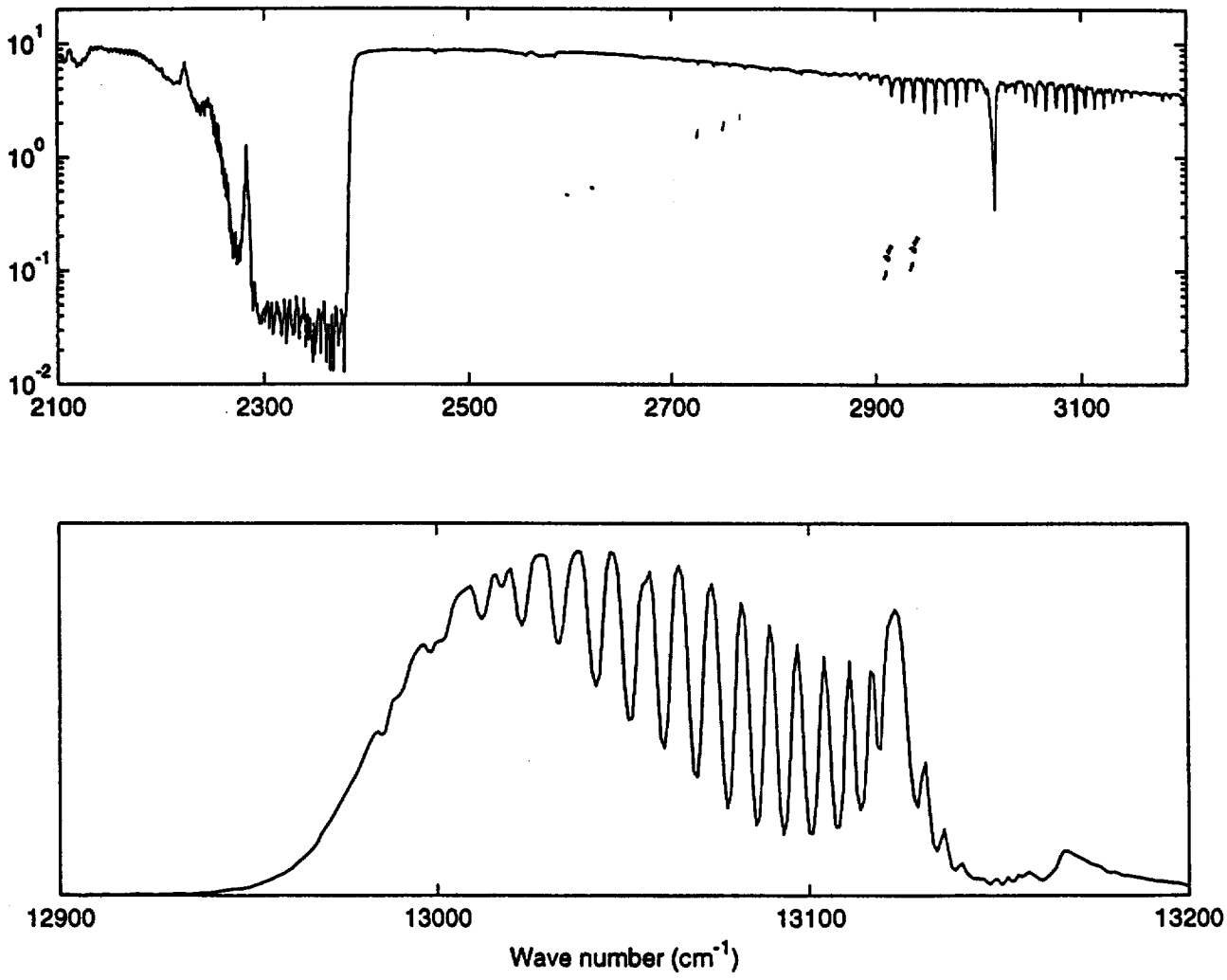
10^{1}
10^{0}
10^{-1}
10^{-2}
2100
2300
2500
2700
2900
3100
12900
13000
13100
13200
Wave number (cm^{-1})